



Dual quasibound states in the continuum in compound grating waveguide structures for large positive and negative Goos-Hänchen shifts with perfect reflection

Feng Wu ^{1,*} Ma Luo ¹ Jiaju Wu,² Caifu Fan,² Xin Qi,² Yiran Jian,² Dejun Liu ³ Shuyuan Xiao ^{4,5}
Gengyan Chen ¹ Haitao Jiang ^{2,†} Yong Sun ² and Hong Chen²

¹*School of Optoelectronic Engineering, Guangdong Polytechnic Normal University, Guangzhou 510665, China*

²*MOE Key Laboratory of Advanced Micro-Structured Materials, School of Physics Science and Engineering, Tongji University, Shanghai 200092, China*

³*Department of Physics, Shanghai Normal University, Shanghai 200234, China*

⁴*Institute for Advanced Study, Nanchang University, Nanchang 330031, China*

⁵*Jiangxi Key Laboratory for Microscale Interdisciplinary Study, Nanchang University, Nanchang 330031, China*



(Received 3 June 2021; accepted 6 August 2021; published 23 August 2021)

Based on the selective excitations of the forward and backward propagating resonant guided modes, we achieve *dual* bound states in the continuum (*dual* BICs) in a compound grating waveguide structure composed of a four-part periodic grating layer and a waveguide layer. Assisted by the quasi-BIC corresponding to forward propagating resonant guided mode (quasi-BIC 1) and the one corresponding to backward propagating resonant guided mode (quasi-BIC 2), large *positive* and *negative* GH shifts can be simultaneously realized. Also, in contrast to the GH shift enhanced by conventional transmission-type resonance, large positive and negative GH shifts assisted by dual quasi-BICs possess 100% reflectance, which can be more easily detected and utilized. Our work provides a route to design GH-shift-based high-performance sensors, wavelength division (de)multiplexers and light storage devices.

DOI: [10.1103/PhysRevA.104.023518](https://doi.org/10.1103/PhysRevA.104.023518)

I. INTRODUCTION

In recent years, a kind of special bound states called bound states in the continuum (BICs) have attracted researchers' interest since they are perfectly confined states without any radiation [1–3]. In 1929, von Neumann and Wigner found that under some artificial potential functions, the single-particle Schrödinger equation could possess bound solutions with discrete eigenvalues embedded in the continuum energy spectrum [4]. This work can be regarded as the origin of the concept of BICs. In 1985, Friedrich and Wintgen proposed a general method to realize BICs in quantum systems based on a two-level non-Hermitian Hamiltonian [5]. The Friedrich-Wintgen approach was theoretically extended to optical systems by Bulgakov and Sadreev in 2008 [6]. After three years, optical BICs were experimentally observed by Plotnik *et al.* [7]. True optical BICs with infinite Q factor are mathematical objects, which cannot be utilized physically. Nevertheless, optical quasi-BICs with ultralarge Q factors can be physically utilized in various applications, such as lasers [8,9], sensors [10,11], light absorption [12–15], enhancement of harmonic generation [16–20] and wireless power transfers [21], due to their strong resonance properties. In the past decade, researchers have proposed lots of microstructures to realize optical quasi-BICs, including photonic crystal slabs [22–29], gratings [30–37], dielectric disk chains [38], and

high-index dielectric resonators [39,40]. Very recently, researchers achieved dual-BICs in dual-grating metamembranes [41] and dual-split ring resonator arrays [42].

When a light beam launches onto the interface between two media, it will undergo a lateral shift from the position predicted by geometrical optics in the incident plane. This lateral shift was observed experimentally by Goos and Hänchen in 1947 and called the Goos-Hänchen (GH) shift [43]. In 1948, Artmann utilized the stationary phase method to prove that the GH shift is proportional to the partial derivative of the reflection phase to the incident angle [44]. If one could realize strong optical resonance with a high- Q factor, reflection phase will dramatically vary around the resonant angle and lead to a large GH shift [45]. Over the past two decades, various resonant microstructures have been proposed to enhance the GH shift, including surface plasmon resonators [46], Bloch surface wave resonators [47], metal cladding waveguides [48], epsilon-near-zero metamaterial slabs [49,50], defective photonic crystals [51], photonic crystal heterostructures [52], and graphene-based structures [53,54]. According to the sign, GH shifts can be divided into two classes: positive GH shifts and negative GH shifts. For most of practical application scenarios, such as sensing and wavelength division (de)multiplexing, positive GH shift is more desirable because the reflected light beam and the incident light beam can be effectively separated [55–57]. However, for some special practical application scenarios, such as light storage (also called light stopping), negative GH shift is necessary in order to achieve a closed optical path [58–60]. Therefore, in addition to realize large positive GH shift, realizing large negative GH shift has also attracted researchers' great interests [61–67].

*fengwu@gpnu.edu.cn

†jiang-haitao@tongji.edu.cn

Very recently, researchers achieved a *single* quasi-BIC in compound grating waveguide structure based on the selective excitation of the resonant guided mode [68]. Assisted by quasi-BIC with ultrastrong resonance, the GH shift can be greatly enhanced to larger than three orders of wavelength [68]. Besides, different from the large GH shift based on conventional transmission-type resonance [46–54], the maximum GH shift assisted by quasi-BIC is located at the reflectance peak with perfect reflection, which can be more easily detected in the experiment. Nevertheless, in Ref. [68], researchers only investigated the selective excitation of the forward propagating resonant guided mode and realized a large positive GH shift. In this paper, we start from the guided mode resonance condition in the compound grating waveguide structure composed of a four-part periodic grating layer and a waveguide layer and then simultaneously achieve selective excitations of the *forward* and *backward* propagating resonant guided modes. By tuning the asymmetric geometric parameter, the four-part periodic grating reduces to the two-part periodic grating with half grating constant. As a result, the previously excitable odd-order resonant guided modes cannot be excited and finally become BICs. Our work shows that under normal incidence, the odd-order forward and backward propagating resonant guided modes are degenerate since the tangential component of the incident wave vector is zero. However, under oblique incidence, the degeneracy of the odd-order forward and backward propagating resonant guided modes is eliminated since the tangential component of the incident wave vector is not zero, leading to *dual* BICs. Interestingly, assisted by the quasi-BIC corresponding to odd-order *forward* propagating resonant guided mode (quasi-BIC 1), we achieve a large *positive* GH shift. Nevertheless, assisted by the quasi-BIC corresponding to odd-order *backward* propagating resonant guided mode (quasi-BIC 2), we also achieve a large *negative* GH shift. To sum up, we realize dual BICs in the compound grating waveguide structures based on the selective excitations of the forward and backward propagating resonant guided mode. Assisted by dual quasi-BICs with ultrahigh Q factors, we simultaneously achieve large *positive* and *negative* GH shifts. Although large positive and negative GH shifts have been simultaneously achieved based on the transmission-type resonances in some published works [46,67], here the large *positive* and *negative* GH shifts possess 100% reflectance, which can be more easily detected and utilized. Our work provides a route to design GH-shift-based high-performance sensors, wavelength division (de)multiplexers as well as light storage devices.

This paper is organized as follows. In Sec. II, we analyze the guided mode resonance (GMR) condition in the compound grating waveguide structure. In Sec. III, we discuss the physical mechanism of single and dual BICs in the compound grating waveguide structure based on the GMR condition. In Sec. IV, we utilize the dual quasi-BICs with ultrahigh Q factors to simultaneously achieve large positive and negative GH shifts. Finally, the conclusion is given in Sec. V.

II. GMR CONDITION IN COMPOUND GRATING WAVEGUIDE STRUCTURE

Figure 1 shows the unit cell of the compound grating waveguide structure composed of a four-part periodic grating

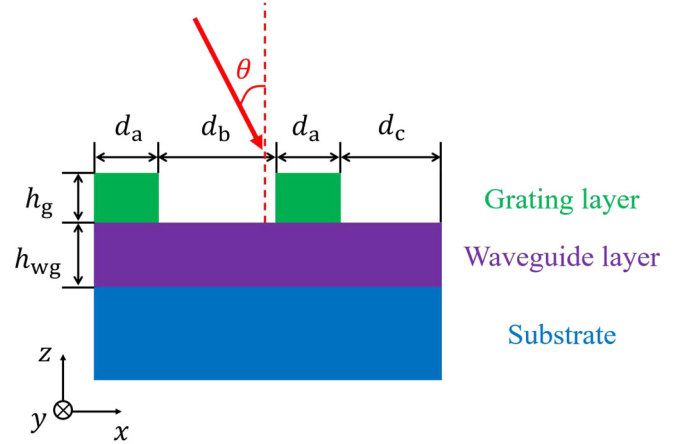


FIG. 1. Schematic of the unit cell of the compound grating waveguide structure. The first layer is a four-part periodic photoresist grating layer with the period Λ and the height h_g . The widths of the first and third parts are the same value d_a while those of the second and fourth parts are $d_b = d_0 + \Delta d$ and $d_c = d_0 - \Delta d$, respectively. The second layer is a HfO_2 waveguide layer with the height h_{wg} . A TE-polarized plane wave is obliquely launched onto the structure with an incident angle θ .

layer and a waveguide layer. The first layer is a four-part periodic grating layer with the grating period $\Lambda = 500$ nm and the height $h_g = 160$ nm. The first and third parts of the unit cell are made of photoresist with the refractive index $n_g = 1.63$ [69], while the second and fourth parts are made of air. The widths of the first and third parts are the same value d_a while those of the second and fourth parts are $d_b = d_0 + \Delta d$ and $d_c = d_0 - \Delta d$, respectively. Here we set $d_a = 0.15\Lambda = 75$ nm and $d_0 = 0.35\Lambda = 175$ nm. An asymmetric geometric parameter $\alpha = \Delta d/d_0 \in [-1, 1]$ is defined to reflect the difference between the second and fourth parts of the unit cell. The second layer is a HfO_2 waveguide layer with the refractive index $n_{wg} = 1.98$ [69] and the height $h_{wg} = 270$ nm. The third layer is a fused-silica substrate with the refractive index $n_s = 1.48$ [69]. This structure can be fabricated by deposition of a layer of HfO_2 on a fused-silica substrate by electron-beam evaporation and subsequent recording of a holographic grating in photoresist on top of the HfO_2 layer [69]. Without loss of generality, we only consider that a transverse electric (TE) polarized plane wave (electric field is parallel to the y direction) obliquely launches onto the structure with an incident angle θ .

Then, we begin to analyze the GMR condition of the proposed structure. The tangential component of the wave vector in the system can be denoted by k_x . In the incident medium (air), k_x can be expressed as $k_x = k_{0x} = k_0 \sin \theta$, where $k_0 = \omega/c$ is the wave vector in the air. ω is the angular frequency and c is the light speed in the air. In the waveguide layer, k_x can be expressed as $k_x = \beta$, where β represents the propagating constant of the guided mode. Without the grating layer, the incident light *cannot* couple with the guided mode because the dispersion relation of the guided mode lies below the light cone of the air ($\beta > k_{0x}$). With the grating layer, the incident light can couple with the guided mode at some specific

frequencies due to the grating-induced reciprocal lattice vector. This phenomenon is called GMR [70,71].

When the asymmetric geometric parameter $\alpha \neq 0$, the widths of the second part $d_b = d_0 + \Delta d$ and the fourth parts $d_c = d_0 - \Delta d$ are different. Therefore, the grating layer is a four-part periodic grating with the period Λ . In the grating layer, k_x can be expressed as $k_x = k_{x,i} = k_{0x} - i \cdot 2\pi/\Lambda$ ($i = \pm 1, \pm 2, \dots$), where $i \cdot 2\pi/\Lambda$ denotes the reciprocal lattice vector induced by the grating. For the compound grating waveguide structure, the main functionality of the top grating layer is to provide the additional wave vector while the main functionality of the waveguide layer is to provide the guided mode [17]. Therefore, the GMR condition can be approximately expressed as [17]

$$k_{x,i} = k_0 \sin \theta - i \frac{2\pi}{\Lambda} = \beta \quad (i = \pm 1, \pm 2, \dots) \quad (1)$$

Without loss of generality, here we only consider the TE_0 guided mode. The dispersion relation of the TE_0 guided mode in the waveguide layer can be determined by [72]

$$h_{\text{wg}} \sqrt{k_0^2 n_{\text{wg}}^2 - \beta^2} = \text{atan} \left(\frac{\sqrt{\beta^2 - k_0^2 n_0^2}}{\sqrt{k_0^2 n_{\text{wg}}^2 - \beta^2}} \right) + \text{atan} \left(\frac{\sqrt{\beta^2 - k_0^2 n_s^2}}{\sqrt{k_0^2 n_{\text{wg}}^2 - \beta^2}} \right). \quad (2)$$

However, when the asymmetric geometric parameter $\alpha = 0$, the widths of the second part $d_b = d_0 + \Delta d$ and the fourth parts $d_c = d_0 - \Delta d$ are identical. Therefore, the four-part periodic grating reduces to a two-part periodic grating with the new period $\Lambda' = \Lambda/2$. The grating-induced reciprocal lattice vector doubles. In the grating layer, k_x can be expressed as $k_x = k'_{x,i} = k_{0x} - i' \cdot 4\pi/\Lambda$ ($i' = \pm 1, \pm 2, \dots$). The GMR condition now becomes

$$k'_{x,i} = k_0 \sin \theta - i' \frac{4\pi}{\Lambda} = \beta \quad (i' = \pm 1, \pm 2, \dots) \quad (3)$$

III. SINGLE AND DUAL BICS IN COMPOUND GRATING WAVEGUIDE STRUCTURE

In this section, we begin with the case of a single BIC under normal incidence $\theta = 0^\circ$. We calculate the dispersion relation of the TE_0 guided mode in the HfO_2 waveguide layer based on Eq. (2), as shown by two blue solid lines in Fig. 2(a). The normalized angular frequency is selected to be $\omega_0 = 2\pi c/h_{\text{wg}}$ and the cutoff angular frequency is $\omega_{\text{cutoff}} = 0.125\omega_0$. The right blue solid line ($\beta > 0$) represents the dispersion relation of the forward propagating TE_0 guided mode while the left one ($\beta < 0$) represents the dispersion relation of the backward propagating TE_0 guided mode. The dispersion relation in the incident medium (air) $k_x = k_{0x} = k_0 \sin \theta = 0$ is shown by black solid line in Fig. 2(a). The dispersion relations in the grating layer (for $\alpha \neq 0$) $k_x = k_{x,i} = k_{0x} - i \cdot 2\pi/\Lambda$ ($i = \pm 1, \pm 2$) is also shown by dashed and dotted lines in Fig. 2(a). The dashed lines represent $k_x = k_{x,i}$ ($i = -1, -2$) while the dotted lines represent $k_x = k_{x,i}$ ($i = +1, +2$). The crossing points between the dispersion relations $k_{x,i}$ and β represent the satisfactions of the GMR condition [Eq. (1)],

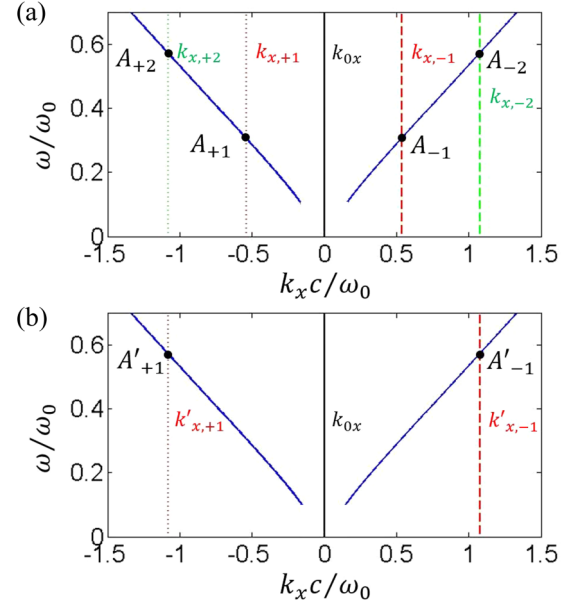


FIG. 2. GMR in the compound grating waveguide structure under normal incidence ($\theta = 0^\circ$). (a) Dispersion relations in the waveguide layer (TE_0 guided mode) $k_x = \beta$ (blue solid line), in the incident medium (air) $k_x = k_{0x} = k_0 \sin \theta$ (black solid line), and $k_x = k_{x,i} = k_{0x} - i \cdot 2\pi/\Lambda$ ($i = \pm 1, \pm 2$) in the grating layer (for $\alpha \neq 0$) (dashed and dotted lines). (b) Dispersion relations in the waveguide layer (TE_0 guided mode) $k_x = \beta$ (blue solid line), in the incident medium (air) $k_x = k_{0x} = k_0 \sin \theta$ (black solid line), and $k_x = k'_{x,i} = k_{0x} - i' \cdot 4\pi/\Lambda$ ($i' = \pm 1$) in the grating layer (for $\alpha = 0$) (dashed and dotted lines).

which can be called the i -th order resonant guided mode. One can see that there are four crossing points: A_{-1} , A_{-2} , A_{+1} , and A_{+2} . Under normal incidence, the forward and backward propagating resonant guided modes are degenerate since $k_{0x} = 0$. The GMR angular frequencies can be obtained as $\omega_{-1} = \omega_{+1} = 0.308\omega_0$ ($\lambda_{-1} = \lambda_{+1} = 876.6$ nm) and $\omega_{-2} = \omega_{+2} = 0.575\omega_0$ ($\lambda_{-2} = \lambda_{+2} = 469.6$ nm), respectively.

When the asymmetric geometric parameter $\alpha = 0$, the dispersion relations in the grating layer become $k_x = k'_{x,i} = k_{0x} - i' \cdot 4\pi/\Lambda$ ($i' = \pm 1, \pm 2, \dots$). Now the new dispersion relation $k'_{x,m}$ is completely identical with the previous even-order dispersion relation $k_{x,2m}$ ($m = \pm 1, \pm 2, \dots$). For example, $k'_{x,-1}$ is identical with $k_{x,-2}$ and $k'_{x,+1}$ is identical with $k_{x,+2}$. In Fig. 2(b), red dashed and dotted lines represent $k'_{x,-1}$ and $k'_{x,+1}$. One can see that only two crossing points A'_{-1} (previous A_{-2}) and A'_{+1} (previous A_{+2}) are remained. As the asymmetric geometric parameter α changes from a nonzero value to zero, the odd-order resonant guided mode ($A_{\pm 1}$) cannot be excited and become a dark mode (corresponds to a single BIC) whereas the even-order resonant guided mode ($A_{\pm 2}$) can still be excited.

Based on the rigorous coupled wave analysis (RCWA) [73], we calculate the TE reflectance spectra (zero-order diffraction) around $\lambda_{\pm 1} = 876.6$ nm of the proposed structure as the geometric parameter α decreases from 1 to 0 under normal incidence, as given in Fig. 3. The reflectance spectra can also be calculated by the spectral element method (SEM) [74–79], which numerically solves the Helmholtz equation of

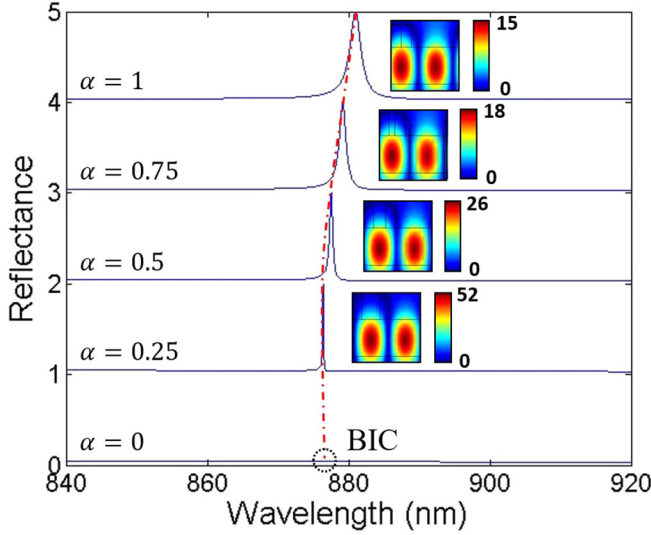


FIG. 3. TE reflectance spectra (zero-order diffraction) around $\lambda_{\pm 1} = 876.6$ nm of the proposed structure for different values of α under normal incidence ($\theta = 0^\circ$). The insets represent the electric field distributions ($|E_y|$) at the corresponding reflectance peaks.

the electric field E_y . The geometry is discretized by mesh with quadrilateral elements. Then, the electric field is discretized by the higher order polynomials in each element [74,78]. The numerically approximated electric field is obtained by solving the weak form of the Helmholtz equation. With the sampling density being less than ten points per wavelength, the accuracy of the SEM reaches a level that the relative error is smaller than $1e-3$ [79]. The reflectance is obtained by comparing the Poynting vector of the scattering field and the incident field. The reflectance spectra calculated by the SEM and the RCWA are nearly the same. The comparison between them is provided in Appendix A. Based on the SEM [74–79], the electric field distributions ($|E_y|$) at the corresponding reflectance peaks are plotted in the insets of Fig. 3. The magnitude of the incident electric field is normalized ($|E_y| = 1$). Owing to the GMR effect, the reflectance spectra exhibit asymmetric Fano line shapes. When $\alpha = 1$, the reflectance peak is located at the wavelength $\lambda = 881.0$ nm, which slightly deviates from the ± 1 st order resonant wavelength $\lambda_{\pm 1} = 876.6$ nm predicted by the GMR condition. The reason is that the grating layer above the waveguide layer will slightly affect the propagating constant of the guided mode in the waveguide layer [17]. In addition, owing to the GMR effect, the electric field at the reflectance peak within the waveguide layer is enhanced. As α gradually decreases from unity to near zero, the resonance width of the reflectance peak reduces dramatically due to the decreased coupling between the ± 1 st order evanescent diffraction field and the leaky guided mode [80]. Meanwhile, the electric field becomes more localized in the waveguide layer, which also indicates that the resonance becomes stronger. As α decreases to zero, the resonance width vanishes completely since the ± 1 st order resonant guided mode $A_{\pm 1}$ cannot be excited, which indicates that a single BIC appears.

Then, we discuss the case of dual BICs under oblique incidence. The incident angle is arbitrary selected as $\theta = 3^\circ$.

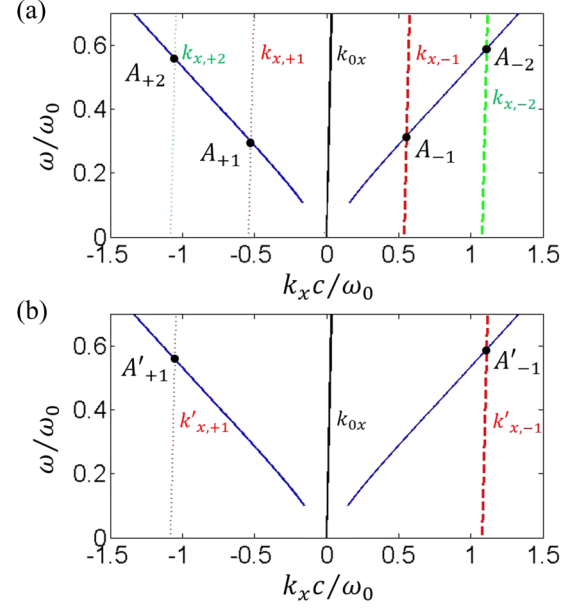


FIG. 4. GMR in the compound grating waveguide structure under oblique incidence ($\theta = 3^\circ$). (a) Dispersion relations in the waveguide layer (TE_0 guided mode) $k_x = \beta$ (blue solid line), in the incident medium (air) $k_x = k_{0x} = k_0 \sin \theta$ (black solid line), and $k_x = k_{x,i} = k_{0x} - i \cdot 2\pi/\Lambda$ ($i = \pm 1, \pm 2$) in the grating layer (for $\alpha \neq 0$) (dashed and dotted lines). (b) Dispersion relations in the waveguide layer (TE_0 guided mode) $k_x = \beta$ (blue solid line), in the incident medium (air) $k_x = k_{0x} = k_0 \sin \theta$ (black solid line), and $k_x = k'_{x,i} = k_{0x} - i' \cdot 4\pi/\Lambda$ ($i' = \pm 1$) in the grating layer (for $\alpha = 0$) (dashed and dotted lines).

Different from normal incidence, the dispersion relation in the incident medium (air) now becomes $k_x = k_{0x} = k_0 \sin \theta \neq 0$, as shown by black solid lines in Fig. 4. The dispersion relations of the TE_0 guided modes in the HfO_2 waveguide layer based on Eq. (2) are also shown by blue solid lines in Fig. 4. For $\alpha \neq 0$, the dispersion relations in the grating layer $k_x = k_{x,i} = k_{0x} - i \cdot 2\pi/\Lambda$ ($i = \pm 1, \pm 2$) is also shown by dashed and dotted lines in Fig. 4(a). The dashed lines represent $k_x = k_{x,i}$ ($i = -1, -2$) while the dotted lines represent $k_x = k_{x,i}$ ($i = +1, +2$). One can see that there are four crossing points: A_{-1} , A_{-2} , A_{+1} , and A_{+2} . Under oblique incidence, the degeneracy of the forward and backward propagating resonant guided modes is eliminated since $k_{0x} \neq 0$, which is the key for realizing dual BICs. The GMR angular frequencies now becomes four values: $\omega_{-1} = 0.317\omega_0$ ($\lambda_{-1} = 851.7$ nm), $\omega_{+1} = 0.301\omega_0$ ($\lambda_{+1} = 897.0$ nm), and $\omega_{-2} = 0.590\omega_0$ ($\lambda_{-2} = 457.6$ nm), and $\omega_{+2} = 0.561\omega_0$ ($\lambda_{+2} = 481.3$ nm), respectively.

When the asymmetric geometric parameter $\alpha = 0$, the dispersion relations in the grating layer become $k_x = k'_{x,i} = k_{0x} - i' \cdot 4\pi/\Lambda$ ($i' = \pm 1, \pm 2, \dots$). Now the new dispersion relation $k'_{x,m}$ is completely identical with the previous even-order dispersion relation $k_{x,2m}$ ($m = \pm 1, \pm 2, \dots$). For example, $k'_{x,-1}$ is identical with $k_{x,-2}$ and $k'_{x,+1}$ is identical with $k_{x,+2}$. In Fig. 4(b), red dashed and dotted lines represent $k'_{x,-1}$ and $k'_{x,+1}$. One can see that only two crossing points A'_{-1} (previous A_{-2}) and A'_{+1} (previous A_{+2}) are remained. As the asymmetric geometric parameter α changes from a

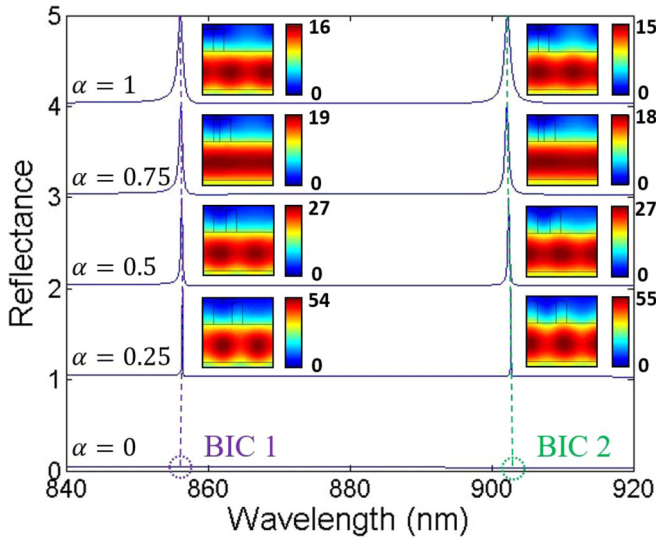


FIG. 5. TE reflectance spectra (zero-order diffraction) around $\lambda_{-1} = 851.7$ nm and $\lambda_{+1} = 897.0$ nm of the proposed structure for different values of α under oblique incidence ($\theta = 3^\circ$). The insets represent the electric field distributions ($|E_y|$) at the corresponding reflectance peaks.

nonzero value to zero, both -1 st and $+1$ st order resonant guided modes (A_{-1} and A_{+1}) cannot be excited and become two dark modes (correspond to dual BICs) whereas both -2 st and $+2$ st order resonant guided modes (A_{-2} and A_{+2}) can still be excited.

Based on the RCWA [73], we calculate the TE reflectance spectra (zero-order diffraction) around $\lambda_{-1} = 851.7$ nm and $\lambda_{+1} = 897.0$ nm of the proposed structure as the geometric parameter α decreases from 1 to 0 under oblique incidence ($\theta = 3^\circ$), as given in Fig. 5. The reflectance spectra can also be calculated by the SEM [74–79], as shown in Appendix A. The reflectance spectra calculated by the RCWA and the SEM are nearly the same. Based on the SEM [74–79], the electric field distributions ($|E_y|$) at the corresponding reflectance peaks are plotted in the insets of Fig. 5. The magnitude of the incident electric field is normalized. When $\alpha = 1$, one can see that there are two Fano-type reflectance peaks. The left

reflectance peak is located at the wavelength $\lambda_1 = 856.1$ nm, which slightly deviates from the -1 st order resonant wavelength $\lambda_{-1} = 851.7$ nm predicted by the GMR condition. The right reflectance peak is located at the wavelength $\lambda_2 = 902.2$ nm, which slightly deviates from the $+1$ st order resonant wavelength $\lambda_{+1} = 897.0$ nm predicted by the GMR condition. In addition, owing to the GMR effect, the electric fields within the waveguide layer at two reflectance peaks are both enhanced. It should be noted that the electric field distribution is quite different from that under normal incidence since the spectrum of the one-dimensional subwavelength grating is angle sensitive [69,81]. As α gradually decreases from unity to near zero, both the resonance widths of two reflectance peaks reduces dramatically due to the decreased coupling between the ± 1 st order evanescent diffraction field and the leaky guided mode [80]. Meanwhile, the electric fields become more localized in the waveguide layer, which also indicates that the resonances become stronger. As α decreases to zero, both the resonance widths of two reflectance peaks vanishes completely since the -1 st and $+1$ st order resonant guided modes A_{-1} and A_{+1} cannot be excited, which indicates that dual BICs appear.

Furthermore, we calculate the Q factors of two reflectance peaks as a function of the asymmetric geometric parameter α , as, respectively, shown in Figs. 6(a) and 6(b). The Q factor is calculated by $Q = f_{\text{Peak}}/\Delta f$, where f_{Peak} is the frequency of the reflectance peak and Δf is the full width at half maximum. Owing to the geometric symmetry of the structure (see Fig. 1), the Q factor for α is identical to that for $-\alpha$. When $\alpha = \pm 1$, the Q factor of the left reflectance peak is only 9.5×10^2 . As α gradually approaches to near zero, the Q factor increases rapidly. For example, the Q factor reaches 2.8×10^5 in the case of $\alpha = \pm 0.05$. When α is equal to zero, the resonance width vanishes completely and the Q factor becomes infinite, corresponding to a BIC. This BIC can be denoted by BIC 1. When $\alpha = \pm 1$, the Q factor of the right reflectance peak is only 8.3×10^2 . As α gradually approaches to near zero, the Q factor increases rapidly. For example, the Q factor reaches 3.5×10^5 in the case of $\alpha = \pm 0.05$. When α is equal to zero, the resonance width vanishes completely and the Q factor becomes infinite, corresponding to another BIC. This BIC can be denoted by BIC 2.

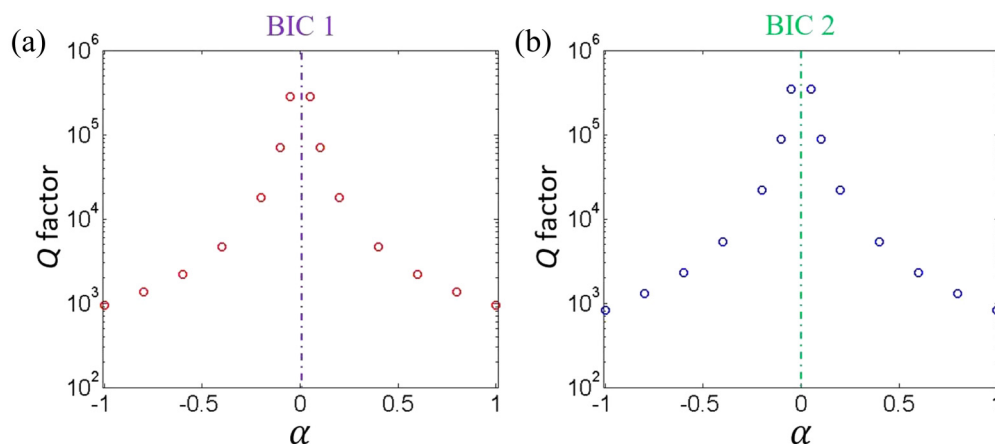


FIG. 6. Q factors of (a) the left reflectance peak and (b) the right one as a function of the asymmetric geometric parameter α .

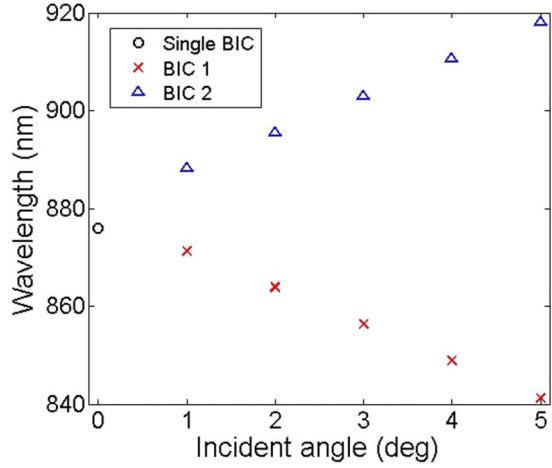


FIG. 7. Wavelengths of BICs as a function of the incident angle.

To sum up, as the incident angle increases from zero degrees, the single BIC turns into dual BICs since the degeneracy of the forward and backward propagating resonant guided modes is eliminated. Figure 7 gives the wavelengths of BICs as a function of the incident angle. When $\theta = 0^\circ$, the single BIC is located at 876.0 nm. As the incident angle increases, the single BIC turns into dual BICs. In detail, BIC 1 shifts towards shorter wavelengths while BIC 2 shifts towards longer wavelengths. When $\theta = 5^\circ$, BIC 1 is located at 841.3 nm while BIC 2 is located at 918.1 nm. As the incident angle increases, the difference between the wavelengths of BIC 1 and BIC 2 becomes larger.

IV. LARGE POSITIVE AND NEGATIVE GH SHIFTS ASSISTED BY DUAL QUASI-BICS

In this section, we utilize dual quasi-BICs to achieve large positive and negative GH shifts. The asymmetric geometric parameter is selected as $\alpha = 0.25$. From Fig. 5, two quasi-BICs are located at $\lambda_1 = 856.1$ nm and $\lambda_2 = 902.7$ nm under oblique incidence ($\theta = 3^\circ$), respectively. We calculate the corresponding TE reflectance angular spectra based on RCWA [73], as shown in Figs. 8(a) and 8(d), respectively. Owing to the strong resonance property of quasi-BIC and the angle-sensitive property of the grating, the “resonance width” in the angular spectrum is also ultranarrow, which can be utilized to greatly enhance the GH shift. According to the stationary phase method, for an incident light beam whose waist width is much larger than the width of resonance, the GH shift can be approximately calculated by [51,64]

$$S_{GH} = -\frac{\lambda}{2\pi} \frac{\partial \varphi_r}{\partial \theta}, \quad (4)$$

where φ_r represents the reflection phase. In Figs. 8(b) and 8(e), we calculate the corresponding TE reflection phase angular spectra, respectively. Based on Eq. (4), the corresponding GH shift angular spectra are also given in Figs. 8(c) and 8(f), respectively. The black dashed lines represent $S_{GH} = 0$. One can see that the reflection phase changes smoothly when the incident angle is away from the resonance angle $\theta = 3^\circ$. However, the reflection phase changes dramatically around the resonance angle $\theta = 3^\circ$, leading to a large GH shift. Interestingly, assisted by quasi-BIC 1 which corresponds to -1 st order forward propagating resonant guided mode ($\beta > 0$), the sign of the GH shift is positive and the value of the GH shift is greatly enhanced to larger than three

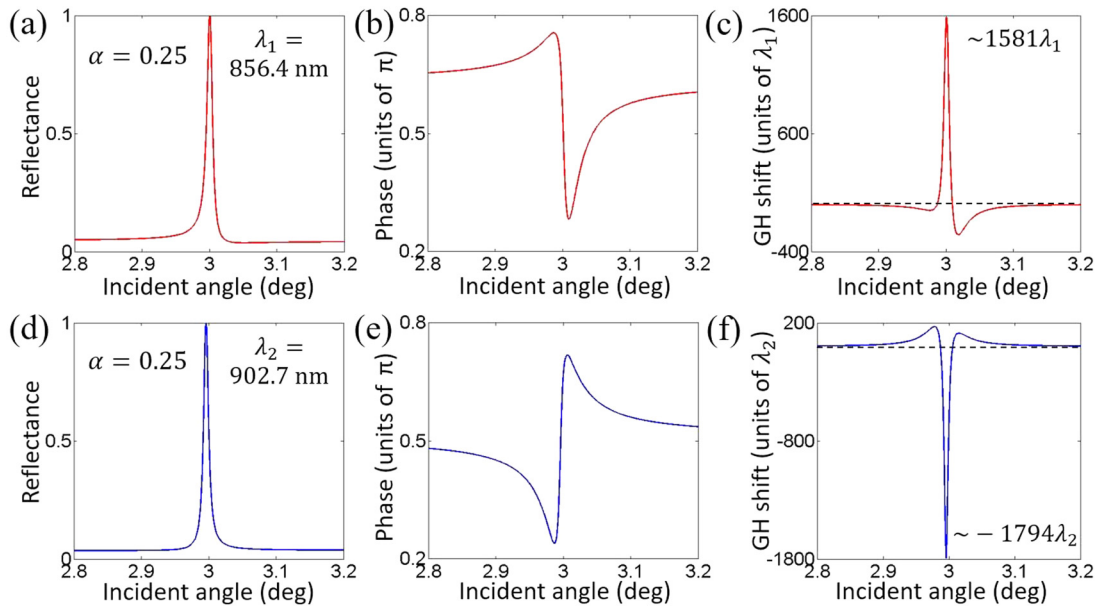


FIG. 8. TE reflectance angular spectra for (a) quasi-BIC 1 $\lambda_1 = 856.4$ nm and (d) quasi-BIC 2 $\lambda_2 = 902.7$ nm. (b) and (e): corresponding TE reflection phase angular spectra. (c) and (f): corresponding GH shift angular spectra. Black dashed lines represent $S_{GH} = 0$. The asymmetric geometric parameter is selected to be $\alpha = 0.25$.

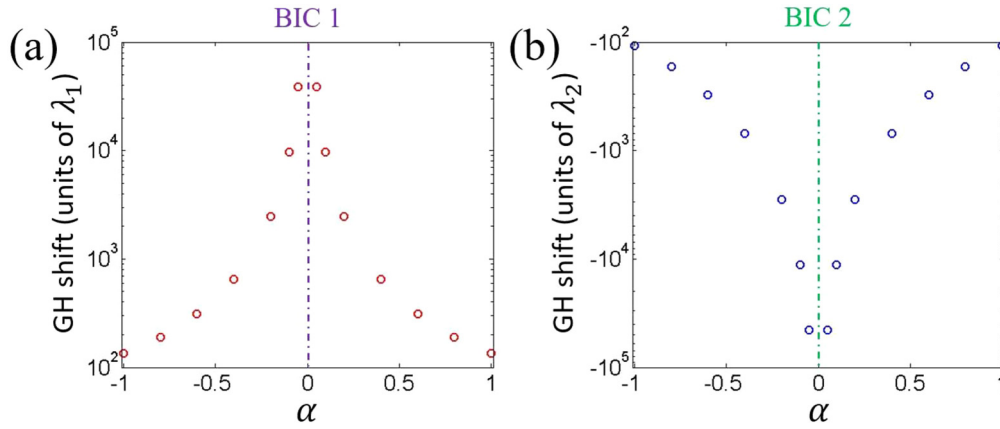


FIG. 9. Maximum GH shifts assisted by (a) quasi-BIC 1 and (b) quasi-BIC 2 as a function of the asymmetric geometric parameter α .

orders of wavelength ($S_{\text{GH}} \approx 1581\lambda_1$). Nevertheless, assisted by quasi-BIC 2 which corresponds to +1st order backward propagating resonant guided mode ($\beta < 0$), the sign of the GH shift is negative and the value of the GH shift is also greatly enhanced to larger than three orders of wavelength ($S_{\text{GH}} \approx -1794\lambda_2$). Assisted by dual BICs, we simultaneously achieve large *positive* and *negative* GH shifts. At the wavelength of quasi-BIC 1, the large positive GH shift can be utilized to realize high-performance sensing [55,56] and wavelength division (de)multiplexing [57]. At the wavelength of quasi-BIC 2, the large negative GH shift can be utilized to realize light stopping [58–60]. Also, different from the large GH shift enhanced by conventional transmission-type resonance [46–54], here the maximum GH shifts assisted by dual quasi-BICs are both located at the reflectance peak with 100% reflectance, which can be more easily detected and utilized.

It should be noted that the calculated maximum GH shifts assisted by dual quasi-BICs are quite large (on the order of $10^3\lambda$). In experiments, the light source is usually a Gaussian beam with a certain waist width, leading to the reduction of the GH shift. The full-wave simulations in previous research showed that when the waist width of the incident Gaussian beam is on the order of the calculated GH shift, the simulated GH shift will be on the order of the calculated GH shift [52]. In Appendix B, we do the full-wave simulation based on the finite element method to confirm this phenomenon. Considering the limitation of the computer memory, we finally choose a moderate GH shift with the asymmetric geometric parameter $\alpha = 1$ to do the full-wave simulation. In other words, in order to obtain a large GH shift on the order of $10^3\lambda$ in experiments, as we calculated by Eq. (4) in Figs. 8(c) and 8(f), the waist width of the incident Gaussian beam should also be on the order of $10^3\lambda$. Although we cannot do the full-wave simulation for such large waist width of the incident Gaussian beam due to the limitation of the computer memory, it is possible to be realized in experiments. Under the current experimental conditions, it is not difficult to create an incident Gaussian beam with a waist width on the order of $10^3\lambda$ [82–84]. Therefore, we believe that the large GH shift on the order of $10^3\lambda$ is possible to be realized in experiments.

Actually, the value of the maximum GH shift is determined by the asymmetric geometric parameter α . As the asymmetric geometric parameter becomes smaller, the resonance becomes stronger and leads to a larger GH shift. Figures 9(a) and 9(b) give the maximum GH shifts assisted by quasi-BIC 1 and quasi-BIC 2 as a function of the asymmetric geometric parameter α . Owing to the geometric symmetry of the structure (see Fig. 1), the maximum GH shift for α is identical to that for $-\alpha$. One can see that the maximum GH shift assisted by quasi-BIC 1 is always positive while the one assisted by quasi-BIC 2 is always negative. When $\alpha = \pm 1$, the maximum GH shift assisted by quasi-BIC 1 is only $1.3 \times 10^2\lambda_1$. As α gradually approaches to near zero, the maximum GH shift increases rapidly. For example, the maximum GH shift is enhanced to larger than four orders of wavelength (reaches $3.8 \times 10^4\lambda_1$) in the case of $\alpha = \pm 0.05$. When $\alpha = \pm 1$, the maximum GH shift assisted by quasi-BIC 2 is only $-1.1 \times 10^2\lambda_2$. As α gradually approaches to near zero, the maximum GH shift increases rapidly. For example, the maximum GH shift is enhanced to larger than four orders of wavelength (reaches $-4.5 \times 10^4\lambda_2$) in the case of $\alpha = \pm 0.05$. It is seen that the dependence of the maximum GH shift on α is quite similar to that of the Q factor on α [see Figs. 6(a) and 6(b)] because the enhancement of the GH shift is closely related to the Q factor of the resonance. It should be noted that the giant GH shift on the order of $10^4\lambda$ is not quite easy to be realized in experiments since it requires an extremely wide incident Gaussian beam.

In experiments, the Q factor of the quasi-BIC is heavily affected by the fabrication quality and finiteness of the sample [32]. Under the current fabrication technique, the experimentally measured Q factor of the subwavelength grating can reach the order of 10^4 [16,22]. Figures 10(a) and 10(b) give the maximum GH shifts assisted by quasi-BIC 1 and quasi-BIC 2 as a function of the Q factor, respectively. The black lines represent the linear fitting lines. One can see that both the maximum GH shifts assisted by quasi-BIC 1 and quasi-BIC 2 are nearly proportional to the Q factor. Substituting the experimental Q factor 1.85×10^4 [16] into the linear fitting results, one can obtain the maximum GH shifts assisted by quasi-BIC 1 and quasi-BIC 2, which still reach $2.5 \times 10^3\lambda_1$ and $-2.4 \times 10^3\lambda_2$, respectively.

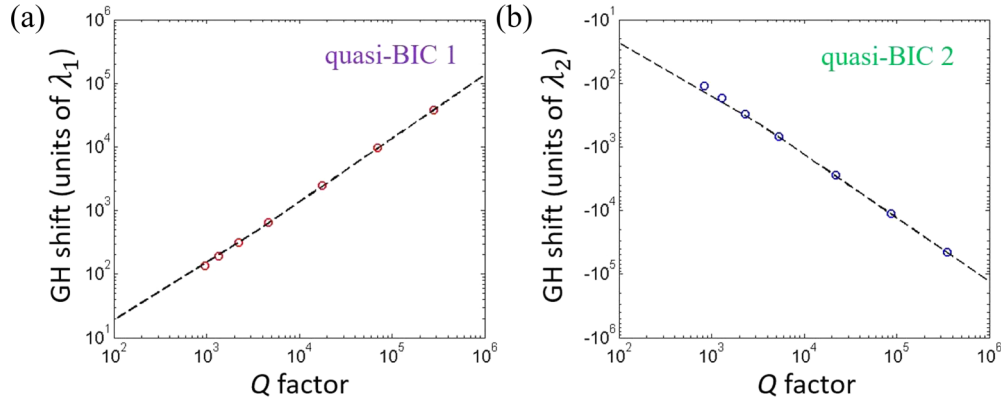


FIG. 10. Maximum GH shifts assisted by (a) quasi-BIC 1 and (b) quasi-BIC 2 as a function of the Q factor.

V. CONCLUSIONS

In summary, we realize dual BICs in the compound structure composed of a four-part periodic grating layer and a waveguide layer based on the selective excitations of the forward and backward propagating resonant guided modes. Assisted by quasi-BIC 1 corresponding to -1 st order forward propagating resonant guided mode, the sign of the GH shift is positive and the value of the GH shift can be greatly enhanced. Nevertheless, assisted by quasi-BIC 2 corresponding to $+1$ st order backward propagating resonant guided mode, the sign of the GH shift is negative and the value of the GH shift can also be greatly enhanced. In addition, the maximal GH shift is located at the reflectance peak with 100% reflectance, which can be easily detected and utilized. Based on the dual-BICs-assisted large positive and negative GH shifts with perfect reflection, high-performance sensors, wavelength division (de)multiplexers and light storage devices could be further designed.

ACKNOWLEDGMENTS

This work is sponsored by the National Key Research Program of China (Grant No. 2016YFA0301101), by the National Natural Science Foundation of China (Grants No.

12104105, No. 91850206, No. 11774261, No. 11974261, No. 61621001, No. 11947065, and No. 11704419), by the Science Foundation of Shanghai (Grants No. 17ZR1443800 and No. 18ZR1442800), by the Shanghai Science and Technology Committee (Grant No. 18JC1410900), by the Shanghai Pujiang Program (Grant No. 20PJ1412200), by the Natural Science Foundation of Jiangxi Province (Grant No. 20202BAB211007), by the Special Project in Key Fields of Universities in Guangdong Province (Grant No. 2020ZDZX3048), by the Start-Up Funding of Guangdong Polytechnic Normal University (Grants No. 2021SDKYA033 and No. 2021SDKYA117), and by the Interdisciplinary Innovation Fund of Nanchang University (Grant No. 2019-9166-27060003).

APPENDIX A: COMPARISON BETWEEN REFLECTANCE SPECTRA CALCULATED BY RCWA AND SEM

In this section, we give the comparison between the TE reflectance spectra (zero-order diffraction) of the proposed structure calculated by the RCWA [73] and the SEM [74–79]. Figures 11(a) and 11(b) correspond to the cases under normal incidence ($\theta = 0^\circ$) and oblique incidence ($\theta = 3^\circ$), respectively. One can see that the reflectance spectra calculated by the RCWA and the SEM are nearly the same.

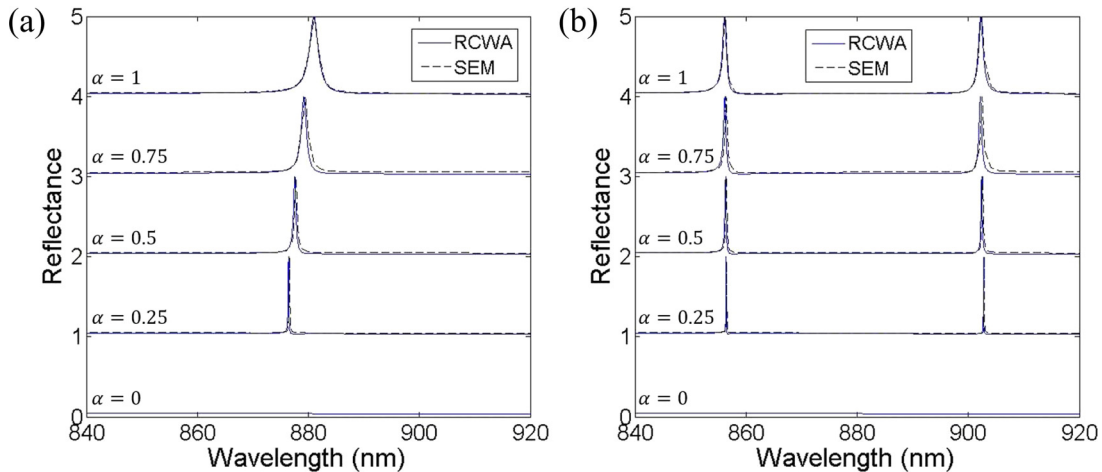


FIG. 11. TE reflectance spectra (zero-order diffraction) of the proposed structure for different values of α calculated by the RCWA and the SEM under (a) normal incidence ($\theta = 0^\circ$) and (b) oblique incidence ($\theta = 3^\circ$).

APPENDIX B: FULL-WAVE SIMULATION UNDER INCIDENCE OF GAUSSIAN BEAM

In this section, we compare the calculated GH shift to the simulated one under the incidence of a Gaussian beam with a finite waist width. Considering the limitation of the computer memory, here we choose a moderate GH shift with the asymmetric geometric parameter $\alpha = 1$ to do the full-wave simulation. Figure 12(a) gives the calculated GH angular spectrum at $\lambda_1 = 856.1$ nm. The calculated maximum GH shift is $S_{GH} \approx 132\lambda_1$ at $\theta = 3^\circ$. Then, we do the full-wave simulation based on the finite element method under the oblique incidence ($\theta = 3^\circ$) of a Gaussian beam with a waist width $100\lambda_1$. The simulated electric field distribution $|E_y|$ is shown in Fig. 12(b). The red arrows represent the central axes of the incident and reflected beams. One can see that the simulated GH shift reaches $S_{GH} \approx 60\lambda_1$, which is on the order of the calculated one (about 0.45 times). Also, the electric field is strongly concentrated within the waveguide layer, which confirms the GMR effect. Finally, the electric field of the reflected beam is strong, which indicates that the reflectance is high.

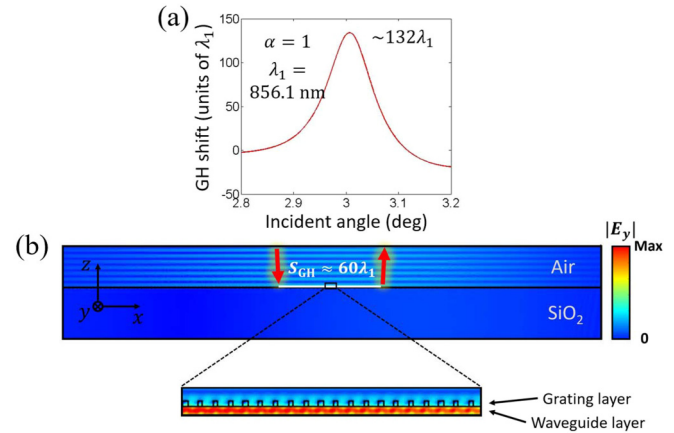


FIG. 12. (a) Calculated GH shift angular spectrum at $\lambda_1 = 856.1$ nm. (b) Simulated electric field distribution under the oblique incidence ($\theta = 3^\circ$) of a Gaussian beam with a waist width $100\lambda_1$. The asymmetric geometric parameter is selected to be $\alpha = 1$.

- [1] C. W. Hsu, B. Zhen, A. D. Stone, J. D. Joannopoulos, and M. Soljačić, Bound state in the continuum, *Nat. Rev. Mater.* **1**, 16048 (2016).
- [2] K. Koshelev, A. Bogdanov, and Y. Kivshar, Meta-optics and bound states in the continuum, *Sci. Bull.* **64**, 836 (2019).
- [3] A. F. Sadreev, Interference traps waves in an open system: Bound states in the continuum, *Rep. Prog. Phys.* **84**, 055901 (2021).
- [4] J. von Neumann, and E. P. Wigner, Über merkwürdige diskrete eigenwerte, *Phys. Z.* **30**, 465 (1929).
- [5] H. Friedrich and D. Wintgen, Physical realization of bound states in the continuum, *Phys. Rev. A* **31**, 3964 (1985).
- [6] E. N. Bulgakov and A. F. Sadreev, Bound states in the continuum in photonic waveguides inspired by defects, *Phys. Rev. B* **78**, 075105 (2008).
- [7] Y. Plotnik, O. Peleg, F. Dreisow, M. Heinrich, S. Nolte, A. Szameit, and M. Segev, Experimental Observation of Optical Bound States in the Continuum, *Phys. Rev. Lett.* **107**, 183901 (2011).
- [8] K. Hirose, Y. Liang, Y. Kurosaka, A. Watanabe, T. Sugiyama, and S. Noda, Watt-class high-power, high-beam-quality photonic-crystal lasers, *Nat. Photonics* **8**, 406 (2014).
- [9] A. Kodigala, T. Lepetit, Q. Gu, B. Bahari, Y. Fainman, and B. Kanté, Lasing action from photonic bound states in continuum, *Nature (London)* **541**, 196 (2017).
- [10] S. Romano, G. Zito, S. Torino, G. Calafiore, E. Penzo, G. Coppola, S. Cabrini, I. Rendina, and V. Mocella, Label-free sensing of ultralow-weight molecules with all-dielectric metasurfaces supporting bound states in the continuum, *Photonics Res.* **6**, 726 (2018).
- [11] X. Chen, W. Fan, and H. Yan, Toroidal dipole bound states in the continuum metasurfaces for terahertz nanofilm sensing, *Opt. Express* **28**, 17102 (2020).
- [12] X. Wang, J. Duan, W. Chen, C. Zhou, T. Liu, and S. Xiao, Controlling light absorption of graphene at critical coupling through magnetic dipole quasibound states in the continuum resonance, *Phys. Rev. B* **102**, 155432 (2020).
- [13] S. Xiao, T. Liu, X. Wang, X. Liu, and C. Zhou, Tailoring the absorption bandwidth of graphene at critical coupling, *Phys. Rev. B* **102**, 085410 (2020).
- [14] S. Cao, H. Dong, J. He, E. Forsberg, Y. Jin, and S. He, Normal-incidence-excited strong coupling between excitons and symmetry-protected quasibound states in the continuum in silicon nitride-WS₂ heterostructures at room temperature, *J. Phys. Chem. Lett.* **11**, 4631 (2020).
- [15] T. Sang, S. A. Dereshgi, W. Hadibrata, I. Tanriover, and K. Aydin, Highly efficient light absorption of monolayer graphene by quasibound state in the continuum, *Nanomaterials* **11**, 484 (2021).
- [16] Z. Liu, Y. Xu, Y. Lin, J. Xiang, T. Feng, Q. Cao, J. Li, S. Lan, and J. Liu, High-*Q* Quasibound States in the Continuum for Nonlinear Metasurfaces, *Phys. Rev. Lett.* **123**, 253901 (2019).
- [17] T. Ning, X. Li, Y. Zhao, L. Yin, Y. Huo, L. Zhao, and Q. Yue, Giant enhancement of harmonic generation in all-dielectric resonant waveguide gratings of quasibound states in the continuum, *Opt. Express* **28**, 34024 (2020).
- [18] K. Koshelev, S. Kruk, E. Melik-Gaykazyan, J. Choi, A. Bogdanov, H. Park, and Y. Kivshar, Subwavelength dielectric resonators for nonlinear nanophotonics, *Science* **367**, 288 (2020).
- [19] J. Wang, M. Clementi, M. Minkov, A. Barone, J. Carlin, N. Grandjean, D. Gerace, S. Fan, M. Galli, and R. Houdré, Doubly resonant second-harmonic generation of a vortex beam from a bound state in the continuum, *Optica* **7**, 1126 (2020).
- [20] Z. Huang, M. Wang, Y. Li, J. Shang, K. Li, W. Qiu, J. Dong, H. Guan, Z. Chen, and H. Lu, Highly efficient second harmonic generation of thin film lithium niobate nanograting near

- bound states in the continuum, *Nanotechnology* **32**, 325207 (2021).
- [21] Y. Xie, Z. Zhang, Y. Lin, T. Feng, and Y. Xu, Magnetic Quasibound States in the Continuum for Wireless Power Transfer, *Phys. Rev. Appl.* **15**, 044024 (2021).
- [22] C. W. Hsu, B. Zhen, J. Lee, S. Chua, S. G. Johnson, J. D. Joannopoulos, and M. Soljačić, Observation of trapped light within the radiation continuum, *Nature (London)* **499**, 188 (2013).
- [23] Y. Yang, C. Peng, Y. Liang, Z. Li, and S. Noda, Analytical Perspective for Bound States in the Continuum in Photonic Crystal Slabs, *Phys. Rev. Lett.* **113**, 037401 (2014).
- [24] K. Koshelev, S. Lepeshov, M. Liu, A. Bogdanov, and Y. Kivshar, Asymmetric Metasurfaces with High- Q Resonances Governed by Bound States in the Continuum, *Phys. Rev. Lett.* **121**, 193903 (2018).
- [25] M. Minkov, I. A. D. Williamson, M. Xiao, and S. Fan, Zero-Index Bound States in the Continuum, *Phys. Rev. Lett.* **121**, 263901 (2018).
- [26] J. Jin, X. Yin, L. Ni, M. Soljačić, B. Zhen, and C. Peng, Topologically enabled ultrahigh- Q guided resonances robust to out-of-plane scattering, *Nature (London)* **574**, 501 (2019).
- [27] S. Li, C. Zhou, T. Liu, and S. Xiao, Symmetry-protected bound states in the continuum supported by all-dielectric metasurfaces, *Phys. Rev. A* **100**, 063803 (2019).
- [28] S. Dai, P. Hu, and D. Han, Near-field analysis of bound states in the continuum in photonic crystal slabs, *Opt. Express* **28**, 16288 (2020).
- [29] B. Wang, W. Liu, M. Zhao, J. Wang, Y. Zhang, A. Chen, F. Guan, X. Liu, L. Shi, and J. Zi, Generating optical vortex beams by momentum-space polarization vortices centred at bound states in the continuum, *Nat. Photonics* **14**, 623 (2021).
- [30] J. W. Yoon, S. H. Song, and R. Magnusson, Critical field enhancement of asymptotic optical bound states in the continuum, *Sci. Rep.* **5**, 18301 (2015).
- [31] F. Monticone and A. Alù, Bound states within the radiation continuum in diffraction gratings and the role of leaky modes, *New J. Phys.* **19**, 093011 (2017).
- [32] Z. F. Sadrieva, I. S. Sinev, K. L. Koshelev, A. Samusev, I. V. Iorsh, O. Takayama, R. Malureanu, A. A. Bogdanov, and A. V. Lavrinenko, Transition from optical bound states in the continuum to leaky resonances: Role of substrate and roughness, *ACS Photonics* **4**, 723 (2017).
- [33] H. M. Doeleman, F. Monticone, W. den Hollander, A. Alù, and A. F. Koenderink, Experimental observation of a polarization vortex at an optical bound state in the continuum, *Nat. Photonics* **12**, 397 (2018).
- [34] E. N. Bulgakov, D. N. Maksimov, P. N. Semina, and S. A. Skorobogatov, Propagating bound states in the continuum in dielectric gratings, *J. Opt. Soc. Am. B* **35**, 1218 (2018).
- [35] S. I. Azzam, V. M. Shalaev, A. Boltasseva, and A. V. Kildishev, Formation of Bound States in the Continuum in Hybrid Plasmonic-Photonic Systems, *Phys. Rev. Lett.* **121**, 253901 (2018).
- [36] S. Joseph, S. Sarkar, S. Khan, and J. Joseph, Exploring the optical bound state in the continuum in a dielectric grating coupled plasmonic hybrid system, *Adv. Opt. Mater.* **9**, 2001895 (2021).
- [37] D. Liu, X. Yu, F. Wu, S. Xiao, F. Itoigawa, and S. Ono, Terahertz high- Q quasibound states in the continuum in laser-fabricated metallic double-slit arrays, *Opt. Express* **29**, 24779 (2021).
- [38] Z. F. Sadrieva, M. A. Belyakov, M. A. Balezin, P. V. Kapitanova, E. A. Nenasheva, A. F. Sadreev, and A. A. Bogdanov, Experimental observation of a symmetric-protected bound state in the continuum in a chain of dielectric disks, *Phys. Rev. A* **99**, 053804 (2019).
- [39] M. V. Rybin, K. L. Koshelev, Z. F. Sadrieva, K. B. Samusev, A. A. Bogdanov, M. F. Limonov, and Y. S. Kivshar, High- Q Supercavity Modes in Subwavelength Dielectric Resonators, *Phys. Rev. Lett.* **119**, 243901 (2017).
- [40] E. Melik-Gaykazyan, K. Koshelev, J. Choi, S. S. Kruk, A. Bogdanov, H. Park, and Y. Kivshar, From Fano to quasi-BIC resonances in individual dielectric nanoantennas, *Nano Lett.* **21**, 1765 (2021).
- [41] H. Hemmati and R. Magnusson, Resonant dual-grating metamembranes supporting spectrally narrow bound states in the continuum, *Adv. Opt. Mater.* **7**, 1900754 (2019).
- [42] L. Cong and R. Singh, Symmetry-protected dual bound states in the continuum in metamaterials, *Adv. Opt. Mater.* **7**, 1900383 (2019).
- [43] F. Goos and H. Hänchen, Ein neuer und fundamentaler Versuch zur Totalreflexion, *Ann. Phys.* **436**, 333 (1947).
- [44] K. Artmann, Berechnung der Seitenversetzung des totalreflektierten Strahles, *Ann. Phys.* **437**, 87 (1948).
- [45] R. Kaiser, Y. Levy, J. Fleming, S. Muniz, and V. S. Bagnato, Resonances in a single thin dielectric layer: Enhancement of the Goos-Hänchen shift, *Pure Appl. Opt.* **5**, 891 (1996).
- [46] X. Yin, L. Hesselink, Z. Liu, N. Fang, and X. Zhang, Large positive and negative lateral optical beam displacements due to surface plasmon resonance, *Appl. Phys. Lett.* **85**, 372 (2004).
- [47] I. V. Soboleva, V. V. Moskalenko, and A. A. Fedyanin, Giant Goos-Hänchen Effect and Fano Resonance at Photonic Crystal Surfaces, *Phys. Rev. Lett.* **108**, 123901 (2012).
- [48] Y. Wang, H. Li, Z. Cao, T. Yu, Q. Shen, and Y. He, Oscillating wave sensor based on the Goos-Hänchen effect, *Appl. Phys. Lett.* **92**, 061117 (2017).
- [49] Y. Xu, C. T. Chan, and H. Chen, Goos-Hänchen effect in epsilon-near-zero metamaterials, *Sci. Rep.* **5**, 8681 (2015).
- [50] J. Wen, J. Zhang, L. Wang, and S. Zhu, Goos-Hänchen shifts in an epsilon-near-zero slab, *J. Opt. Soc. Am. B* **34**, 2310 (2017).
- [51] L. Wang and S. Zhu, Giant lateral shift of a light beam at the defect mode in one-dimensional photonic crystals, *Opt. Lett.* **31**, 101 (2006).
- [52] J. Wu, F. Wu, K. Lv, Z. Guo, H. Jiang, Y. Sun, Y. Li, and H. Chen, Giant Goos-Hänchen shift with a high reflectance assisted by interface states in photonic heterostructures, *Phys. Rev. A* **101**, 053838 (2020).
- [53] Y. Chen, Y. Ban, Q. Zhu, and X. Chen, Graphene-assisted resonant transmission and enhanced Goos-Hänchen shift in a frustrated total internal reflection configuration, *Opt. Lett.* **41**, 4468 (2016).
- [54] W. Zhen and D. Deng, Goos-Hänchen shifts for Airy beams impinging on graphene-substrate surfaces, *Opt. Express* **28**, 24104 (2020).
- [55] X. Wang, C. Yin, J. Sun, H. Li, Y. Wang, M. Ran, and Z. Cao, High-sensitivity temperature sensor using the ultrahigh order

- mode-enhanced Goos-Hänchen effect, *Opt. Express* **21**, 13380 (2013).
- [56] X. Wang, M. Sang, W. Yuan, Y. Nie, and H. Luo, Optical relative humidity sensing based on oscillating wave-enhanced Goos-Hänchen shift, *IEEE Photonics Technol. Lett.* **28**, 264 (2016).
- [57] H. Sattari, S. E. Bakhtevan, and M. Sahrai, Proposal for a 1×3 Goos-Hänchen shift-assisted de/multiplexer based on a multilayer structure containing quantum dots, *J. Appl. Phys.* **120**, 133102 (2016).
- [58] K. L. Tsakmakidis, A. D. Boardman, and O. Hess, ‘Trapped rainbow’ storage of light in metamaterials, *Nature (London)* **450**, 397 (2007).
- [59] R. Yang, W. Zhu, and J. Li, Realization of “trapped rainbow” in 1D slab waveguide with surface dispersion engineering, *Opt. Express* **23**, 6326 (2016).
- [60] T. Huang and T. Yen, Experimental demonstration of broadband light trapping by exciting surface modes of an all-dielectric taper, *Sci. Rep.* **9**, 3538 (2019).
- [61] P. R. Berman, Goos-Hänchen shift in negatively refractive media, *Phys. Rev. E* **66**, 067603 (2002).
- [62] H. M. Lai and S. W. Chan, Large and negative Goos-Hänchen shift near the Brewster dip on reflection from weakly absorbing media, *Opt. Lett.* **27**, 680 (2002).
- [63] J. He, J. Yi, and S. He, Giant negative Goos-Hänchen shifts for a photonic crystal with a negative effective index, *Opt. Express* **14**, 3024 (2006).
- [64] L. Wang, H. Chen, and S. Zhu, Large negative Goos-Hänchen shift from a weakly absorbing dielectric slab, *Opt. Lett.* **30**, 2936 (2005).
- [65] X. Chen, L. Wang, and C. Li, Transmission gap, Bragg-like reflection, and Goos-Hänchen shifts near the Dirac point inside a negative-zero-positive index metamaterial slab, *Phys. Rev. A* **80**, 043839 (2009).
- [66] X. Wu, Goos-Hänchen shifts in tilted uniaxial crystals, *Opt. Commun.* **416**, 181 (2018).
- [67] Y. Wong, Y. Miao, J. Skarda, and O. Solgaard, Large negative and positive optical Goos-Hänchen shift in photonic crystals, *Opt. Lett.* **43**, 2803 (2018).
- [68] F. Wu, J. Wu, Z. Guo, H. Jiang, Y. Sun, Y. Li, J. Ren, and H. Chen, Giant Enhancement of the Goos-Hänchen Shift Assisted by Quasibound States in the Continuum, *Phys. Rev. Appl.* **12**, 014028 (2019).
- [69] Z. S. Liu, S. Tibuleac, D. Shin, P. P. Young, and R. Magnusson, High-efficiency guided-mode resonance filter, *Opt. Lett.* **23**, 1556 (1998).
- [70] G. D’Aguanno, D. de Ceglia, N. Mattiucci, and M. J. Bloemer, All-optical switching at the Fano resonances in subwavelength gratings with very narrow slits, *Opt. Lett.* **36**, 1984 (2011).
- [71] T. Sang, S. Cai, and Z. Wang, Guided-mode resonance filter with an antireflective surface consisting of a buffer layer with refractive index equal to that of the grating, *J. Mod. Opt.* **58**, 1260 (2011).
- [72] A. Yariv and P. Yeh, *Optical Waves in Crystals* (Wiley, New York, 1984).
- [73] M. G. Moharam, D. A. Pommet, E. B. Grann, and T. K. Gaylord, Stable implementation of the rigorous coupled-wave analysis for surface-relief gratings: Enhanced transmittance matrix approach, *J. Opt. Soc. Am. A* **12**, 1077 (1995).
- [74] M. Luo, Q. H. Liu, and Z. Li, Spectral element method for band structures of two-dimensional anisotropic photonic crystals, *Phys. Rev. E* **79**, 026705 (2009).
- [75] M. Luo and Q. H. Liu, Spectral element method for band structures of three-dimensional anisotropic photonic crystals, *Phys. Rev. E* **80**, 056702 (2009).
- [76] M. Luo and Q. H. Liu, Accurate Determination of Band Structures of 2D Dispersive Anisotropic, *J. Opt. Soc. Am. A* **26**, 1598 (2009).
- [77] M. Luo and Q. H. Liu, Three-dimensional dispersive metallic photonic crystals with a bandgap and a high cutoff frequency, *J. Opt. Soc. Am. A* **27**, 1878 (2010).
- [78] M. Luo, Q. H. Liu, and J. Guo, A spectral element method calculation of extraordinary light transmission through periodic subwavelength slits, *J. Opt. Soc. Am. B* **27**, 560 (2010).
- [79] M. Luo and Q. H. Liu, Extraordinary transmission of a thick film with a periodic structure consisting of strongly dispersive materials, *J. Opt. Soc. Am. B* **28**, 629 (2011).
- [80] W. Liu, Y. Li, H. Jiang, Z. Lai, and H. Chen, Controlling the spectral width in compound waveguide grating structures, *Opt. Lett.* **38**, 163 (2013).
- [81] C. Wei, S. Liu, D. Deng, J. Shen, J. Shao, and Z. Fan, Electric field enhancement in guided-mode resonance filters, *Opt. Lett.* **31**, 1223 (2006).
- [82] M. Merano, A. Aiello, G. W’t Hooft, M. P. Van Exter, E. R. Eliel, and J. P. Woerdman, Observation of Goos-Hänchen shifts in metallic reflection, *Opt. Express* **15**, 15928 (2007).
- [83] Y. Wan, Z. Zheng, W. Kong, X. Zhao, Y. Liu, Y. Bian, and J. Liu, Nearly three orders of magnitude enhancement of Goos-Hänchen shift by exciting Bloch surface wave, *Opt. Express* **20**, 8998 (2012).
- [84] Y. Wan, Z. Zheng, W. Kong, Y. Liu, Z. Lu, and Y. Bian, Direct experimental observation of giant Goos-Hänchen shifts from bandgap-enhanced total internal reflection, *Opt. Lett.* **36**, 3539 (2011).